Three dimensional flow of liquid transfer between a cavity and a moving roll

Diego M. Campana [a,b,*], Sebastián Ubal [a,b], María D. Giavedoni [a], Fernando A. Saita [a], Marcio S. Carvalho [c,**]

[a] Instituto de Desarrollo Tecnológico para la Industria Química (INTEC-CONICET), Güemes 3450, Santa Fe (3000), República Argentina
[b] CITER (UNER-CONICET), Facultad de Ingeniería, Universidad Nacional de Entre Ríos, Ruta 11, Km. 10, Oro Verde, Entre Ríos (3100), República Argentina
[c] PUC-Rio, Department of Mechanical Engineering, Pontifícia Universidade Católica do Rio de Janeiro (PUC-RIO), Rua Marques de São Vicente 225, Gavea, Rio de Janeiro, RJ 22453-900, Brazil

HIGHLIGHTS

- Full three-dimensional analysis of liquid transfer from a cavity to a rotating roll.
- Transferred liquid volume depends strongly on the capillary number of the process.
- At low capillary number, poor printing placement precision (registration) is attained.
- At high capillary number, registration improves and transferred volume is still high.
- Smaller roll diameter contributes to higher transferred liquid volume.

GRAPHICAL ABSTRACT
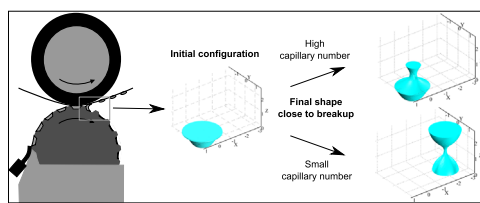
ARTICLE INFO

ABSTRACT

Gravure printing is one of the most promising technologies for high volume production of printed electronics and microscale films and devices. The characteristics of the printed pattern, i.e. ink volume, resolution and pattern placement (registration), are directly related to the fluid mechanics of the liquid transfer process from a cell to a substrate wrapped around a rotating roll; the liquid transfer is mainly controlled by free surfaces and dynamic contact lines. Most of the available analyses are restricted to axisymmetric flows, at which the relative motion between the cavity and the substrate is greatly simplified. Recent results have shown that the use of the complete description of the relative motion in a roll-to-roll process is critical to obtain accurate results on the amount of liquid that is transferred to the substrate. In this work we present an extension of the model describing liquid transfer from a groove to a substrate in a R2R process in order to consider the liquid transfer from a small individual cell; to this end we solve a full 3D free surface flow with moving contact lines. The results show that the liquid transfer dynamics is governed by two different characteristic time scales, one is associated with the contact line motion and the other with liquid filament breakup. Both are dependent on the

* Corresponding author at: CITER (UNER-CONICET), Facultad de Ingeniería, Universidad Nacional de Entre Ríos, Ruta 11, Km. 10, Oro Verde, Entre Ríos (3100), República Argentina.
** Corresponding author.
E-mail addresses: dcampana@santafe-conicet.gov.ar (D.M. Campana), msc@puc-rio.br (M.S. Carvalho).

capillary number. The predictions show how the volume, registration and shape of the printed dot varies with operating conditions and liquid properties. These predictions could be helpful in designing high precision printing operations.

1. Introduction

In the last ten years, the development of novel conductive organic materials together with the need to build electronic circuits on flexible substrates has renewed the attention on printing technologies (Willmann et al., 2014; Kang et al., 2013). The effort has been specially directed to roll-to-roll processes (R2R), mainly due to the potential high production rates. Among the different R2R processes, roto-gravure techniques provide a good compromise between production rate and the required printed pattern resolution (Krebs, 2009). In roto-gravure printing, the pattern to be printed is engraved on the surface of a rotating roll; then, as depicted in Fig. 1a, the pattern is transferred to the substrate by pressing it between the engraved and a second soft roll. The fluid mechanics of liquid bridges with moving contact lines between moving surfaces has been the subject of considerable research (see Kumar (2015) for a review) because it is essential for understanding many aspects involved in printing.

Here we focus on the particular aspect of liquid transfer from a single cavity to a flat surface. Because of the small scale, the complex relative motion between two rotating surfaces and the relative high speed of these surfaces, flow visualization is extremely challenging. A common approach is to use scaled-up cavities with simplified kinematics. For example, Yin and Kumar (2006) used a groove with trapezoidal cross section having a width and depth of approximately 1 mm to visualize the liquid transfer from the groove to a curved surface (or a rubber-covered roller) moving horizontally over the groove. They found that the volume of liquid remaining inside the groove increases as a power-law function with the capillary number, while the flow visualization suggested an emptying mechanism mainly controlled by capillary forces. This observation was more remarkable when small gaps were formed between the moving surface and the cavity corners, because in this case high capillary pressure gradients were produced in the menisci driving liquid outside the cavity. Despite the

simplified kinematics used and the fact that the range of Stokes number (ratio between gravitational and viscous forces) in the experiments was orders of magnitude higher than in actual gravure printing process, flow visualization revealed the importance of contact line motion on the liquid transfer process. Other experiments using scaled-up gravure cells presented by Chuang et al. (2008) and Lee et al. (2012) show similar results. More recently, Sankaran and Rothstein (2012) used axisymmetric trapezoidal cavities (width and depth ~2 and 1 mm, respectively) to study the effect of the vertical stretching velocity and fluid rheology on the liquid transfer process. The results indicate that, with pure vertical relative motion between the surfaces, the volume of transferred liquid rises with capillary number up to a plateau. As was discussed in a subsequent related work (Lee et al., 2013), the appearance of this plateau was probably due to limitations of the experimental setup for working at high speeds. They also showed that the elastic stresses, which occur when viscoelastic liquids are used, delay the filament breakup. Because gravity had an important effect on the experiments, the impact of the viscoelasticity upon the transfer process was highly dependent on the setup configuration. Despite the interesting results of the aforementioned works, at the real scale of the problem (micrometers), gravity is certainly negligible; therefore, modeling can be a powerful tool to understand the fundamentals of the flow.

Powell et al. (2002) presented a finite element model to study the liquid removal from a groove by the action of a passing meniscus. Inspired in this work, Hoda and Kumar (2008) solved a similar problem but used the boundary integral method to study the liquid removal. The contact line was fixed at the moving plate and it was allowed to slip along the cavity wall. The results revealed that the amount of liquid left inside the groove was a strong function of the kinematics imposed by the moving plate.

Dodds et al. (2009, 2011) presented a 2D axisymmetric analysis of the liquid transfer between a fixed single trapezoidal cavity and a surface moving vertically away from it (see Fig. 1b), to determine
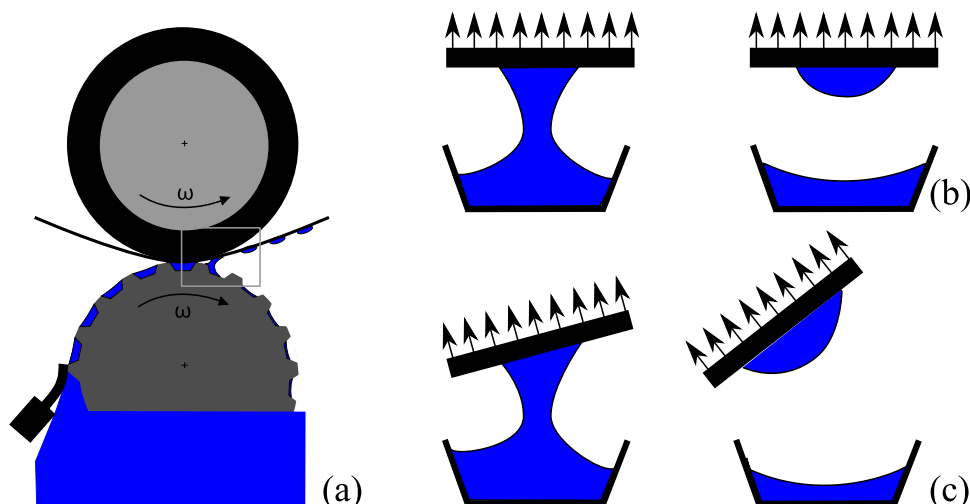

Fig. 1. (a) Sketch of a roto-gravure printing system; (b) simpler model for the liquid transfer between a single cavity and substrate, considering a one dimensional surface motion; (c) a more realistic model, where the surfaces motion tends to mimic the roll-to-roll kinematics.

the pick-out liquid fraction ϕ, defined as the ratio between the liquid volume transferred to the substrate and the total liquid volume initially inside the cavity. Solving the governing equations using the Galerkin finite element method (GFEM), Dodds et al. (2011) explored the effect of wettability (contact angles) and cavity aspect ratio (width / depth) on ϕ. Higher values of ϕ were obtained for non-wetting cavity surface ($\theta_c > 90°$) and wetting substrate ($\theta_p < 90°$). In addition, they showed that ϕ rises as the cavity aspect ratio increases and suggested that ϕ should fall as the cavity wall becomes steeper.

A closer look at the relative motion between the cavity and the substrate reveals that the kinematics is more complex than the simple one-directional extension motion (Fig. 1b) considered in the previous analyses. As was mentioned, Hoda and Kumar (2008) showed that lateral (shear) and rotational displacements of the substrate relative to the cavity result in important changes on the cavity emptying process. Recently, Campana and Carvalho (2014) used a similar approach to that presented by Dodds et al. (2009, 2011) to study the liquid transfer from grooves by introducing the complete kinematic description (sketched in Fig. 1c) of the relative motion that occurs in a R2R configuration. This approach allowed to analyze the effects that operating and geometric parameters, such as roll diameter and velocities have on the transfer process. They found that the relative rotational and lateral velocities between the cavity and substrate surfaces enhance the liquid displacement and increase the liquid transfer fraction ϕ, when compared to the simpler one-directional motion. The predictions show a non-monotonic behavior of ϕ as a function of the capillary number $Ca = \mu V / \sigma$ (μ being the liquid viscosity, V the stretching reference velocity and σ the surface tension), represented schematically in Fig. 2. In particular, for $Ca < 0.1$ the authors observed that the contact lines are able to move out of the cavity; this is due to increased capillary forces. If the contact line motion is faster than the fluid stretching ($Ca \leq 0.01$), the filament begins to break as if it were being stretched between two flat surfaces. When this occurs ϕ approaches 0.5 because strong rotational velocities are needed to disrupt the symmetry of the flow (Dodds et al., 2012). However, if the filament breakup begins when part of fluid is still inside the cavity, more fluid will be transferred to the substrate

and $\phi > 0.5$. For $Ca > 0.1$, the filament breakup occurs without significant contact line motion. In this case, ϕ rises with capillary number. The competition between these two characteristic time scales explains the non-monotonic variation of the liquid transfer fraction ϕ with Ca, sketched in Fig. 2. This behavior is not observed when the liquid transfer kinematics is modeled only by an extensional motion.

The 2D planar flow model of Campana and Carvalho (2014) that considers the complete kinematic description of a R2R process can only be used to calculate the liquid transfer from straight grooves. To model the process by which liquid is removed from trapezoidal cavities and transferred to a substrate wrapped around a roll considering the full R2R kinematics, a 3D flow model with moving contact lines is needed. Probably, the small number of works in which those models are discussed is related to their considerable complexity. Among them we can cite the contributions by Cairncross et al. (2000), Baer et al. (2000), Dodds et al. (2012), and Cen et al. (2014). Cairncross et al. (2000) and Baer et al. (2000) presented a 3D model with moving contact lines using boundary fitted finite element meshes. Dodds et al. (2012) used a 3D finite element model to describe the breakup of a liquid filament between two flat plates moving relative to each other. The numerical technique used in those works can be classified in a group frequently called *interface tracking methods*, because the free surface is defined as a boundary of the flow domain and its position is calculated with the other flow variables. As the interface evolves, the flow domain deforms and suitable techniques must be implemented to calculate and update the computational mesh. Cairncross et al. (2000) and Baer et al. (2000) used a pseudo-solid mesh deforming algorithm while Dodds et al. (2012) implemented an elliptic mesh generation method to compute the node coordinates. In the interface tracking methods, the curvature of the interface is directly evaluated from the nodal position and accurate flow predictions are obtained even when using relatively coarse meshes, providing that the mesh distortion is not so strong. However, coalescence and breakup cannot be modeled with these techniques.

Another example of 3D model with moving contact lines was presented by Cen et al. (2014). They used the finite element method combined with the level-set approach to model the process by which a flexible blade is used to fill a cavity. Their numerical approach follows in the class generally called *interface capturing techniques*. In these methods, the mesh is generally fixed and a scalar field is used to define the different phases present in the flow. The main advantage of these methods is that they are able to handle large interface deformation, such as coalescence and breakup. However, since the interface is defined as an iso-surface (level-set) of the scalar field, the evaluation of the curvature is not as accurate as in interface tracking methods and it is highly dependent on some numerical tuning parameters and mesh refinement.

The aim of the numerical analysis presented by Cen et al. (2014) was to understand how the interface moves and the contact line slips over the cavity walls as a cell is filled with liquid. Their experimental results show that the capillary number, defined using the filling velocity (or tangential roll velocity), is a good indicator of the filling regime. The contact line tends to pin at the cavity corner and only at $Ca < 0.1$ it is able to move over the solid surfaces enabling the complete filling of the cavity. By increasing Ca the filling progressively worsens; moreover, in experiments, air entrapment is observed inside the cavities for the higher capillary numbers considered. With their numerical model, Cen et al. (2014) could reproduce how the interface displaces over the surface, enters the cavity and exits on the other side, filling it completely. However, the technique failed to reproduce how the air is entrapped. They discuss that despite the limited accuracy of the numerical solution, that led to large differences between the time scales predicted by the model and those observed in their
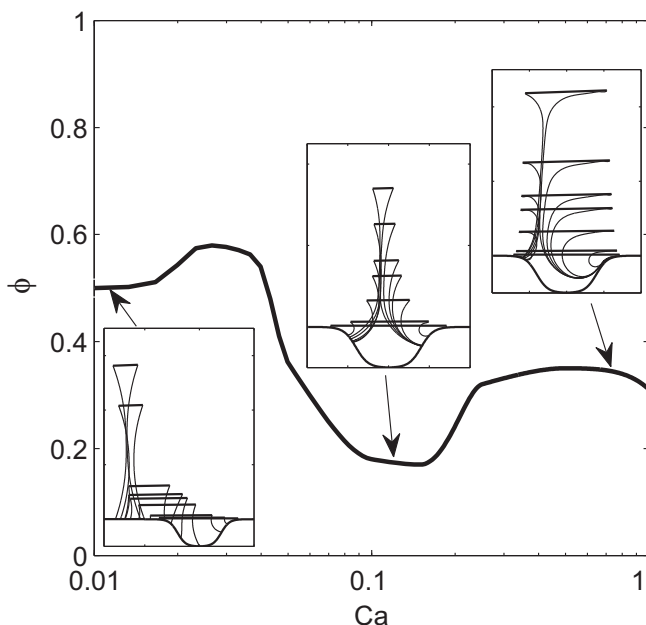

Fig. 2. Sketch of the variation of liquid volume transfer with capillary number for the case of a 2D planar flow (straight groove) analyzed by Campana and Carvalho (2014).

experiments, the model was able to provide physical insights to improve the filling process at high-speed gravure printing.

In summary, the effect of operating conditions and liquid properties on the amount of liquid removed from a single cavity in a gravure printing process remains an open problem. In this work, we extend the previous results of Campana and Carvalho (2014) to a more general situation by solving a new 3D free surface flow model with moving contact lines. Section 2 presents the mathematical model and Section 3, the finite element approach used to solve it. In Section 4, the model is validated by comparing its predictions with available axisymmetric flows; also, the evolution of the liquid filament and liquid transfer fraction are presented for different operating conditions. Finally, Section 5 presents the main conclusions and final remarks.

2. Mathematical model

Fig. 3 represents the cross section (in the $z - x$ plane) of the three-dimensional domain considered to model the liquid transfer between a single cavity and a moving plate. The geometry of the cavity is described by the revolution surface around the z-axis of the cross section defined by the function (Dodds et al., 2009; Campana and Carvalho, 2014):

$$z = f(r) = -\frac{1}{2}\left[1 - \tanh\left(\frac{r - r_c}{r_s}\right)\right] \tag{1}$$

In Eq. (1), the variables are made dimensionless with the cavity depth δ, being $r = \sqrt{x^2 + y^2}$ the distance from a point on the wall to the z-axis and r_c the value of this variable measured at $z = -1/2$. In addition, r_s is a parameter that controls both the curvature of the corners and the steepness of the cavity wall. Sharper corners and steeper cavity walls are obtained by using smaller values of r_s.

There is a fixed frame (x, y, z) with unit vectors $(\mathbf{i}, \mathbf{j}, \mathbf{k})$, attached to the center of the cavity. Although the cavity is perfectly symmetric under z-axis rotation, the liquid bridge is not because the plate has a relative velocity $\mathbf{V}_w(\mathbf{x}, t)$ with components in z and x directions. The dimensionless velocity $\mathbf{V}_w(\mathbf{x}, t)$ of any point lying on the plate, which approximates a R2R kinematics, was derived in detail by Campana and Carvalho (2014):

$$\mathbf{V}_w(\mathbf{x}, t) = [-2\omega R_b \cos^2(\theta) - 2\omega z + \omega A \sin(\theta)]\mathbf{i}$$
$$+ [-2\omega R_b \cos(\theta)\sin(\theta) + 2\omega x - \omega A \cos(\theta)]\mathbf{k},$$
$$A = 2R_b + H_0/\delta - 2R_b \sin(\theta) \equiv 2R_b + H_b - 2R_b \sin(\theta), \tag{2}$$
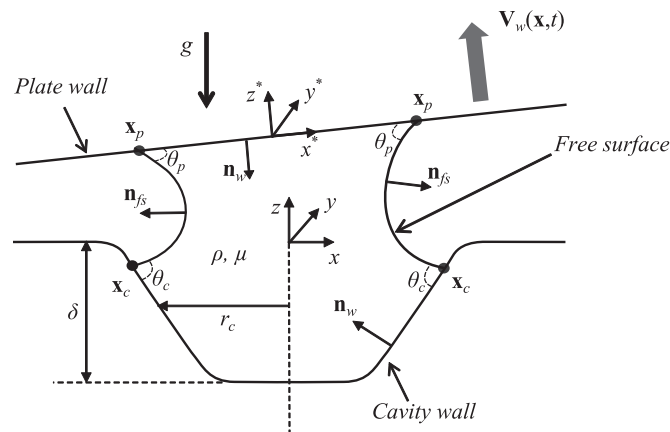

Fig. 3. Sketch of the transversal section ($z - x$ plane) of the flow domain, showing the spatial variables, dimensions and geometric parameters.

where A is the instantaneous gap in units of cavity depth, H_0 is the gap between both surfaces at $t=0$ and the angle θ is given by $\theta = \omega t + \pi/2$, and represents the instantaneous inclination angle of the plate measured from a vertical line in anti-clockwise direction: plate in horizontal position implies $\theta = \pi/2$. Eq. (2) was derived assuming that both rolls have the same radius R and angular speed Ω. The equation was made dimensionless using appropriate length and velocity scales. The cavity depth δ is used as the characteristic length scale. As discussed by Dodds et al. (2009), the stretching vertical velocity V_E at which the surfaces separate represents a convenient characteristic velocity scale of the problem. It is a function of the roll tangential velocity ΩR, the filament length at breakup L_b and the roll radius R. Dodds et al. (2009) have shown that there is an upper limit value for the filament length at breakup, i.e. $L_b \approx 5\delta$ and thus $V_E \approx \Omega R\sqrt{2L_b/R} = \Omega R\sqrt{10\delta/R}$. The dimensionless parameters in Eq. (2) are defined as: $\omega \equiv \Omega\delta/V_E$, $H_b \equiv H_0/\delta$, and $R_b \equiv R/\delta$. It is interesting to observe that with the velocity scale V_E used, the dimensionless angular speed ω can be simplified to $\omega = \sqrt{0.1/R_b}$; hence, this variable is not an independent dimensionless parameter. The dimensionless velocity is a function of the geometric parameters H_b and R_b only.

At $t=0$, the plate above the cavity (which represents the surface of the roll that moves with respect to the engraved roll) is located perfectly horizontal over the cavity at $z = H_b$. Also at $t=0$, the origin of the second frame (x_*, y_*, z_*) attached to the moving plate has coordinates $(x, y, z) = (0, 0, H_b)$. This frame will be used later to represent the printed pattern on the substrate.

A Newtonian liquid with density ρ, viscosity μ and surface tension σ, forms a liquid bridge between the cavity and the top plate. The surrounding gas phase has negligible density and viscosity and a constant pressure $p_0 = 0$, which is taken as reference. At $t=0$ we consider the system in equilibrium; then, the free surface is a static meniscus between the cavity and plate with static contact angles θ_c and θ_p, respectively. The quantities $\mathbf{x}_c$ and $\mathbf{x}_p$ represent the contact line positions along the cavity and plate, respectively.

In a previous work, Campana and Carvalho (2014) argued that for typical cavity sizes in the order of 10 μm and usual fluid properties, gravity force can be safely neglected but the inertial effects can be important depending on the rotational velocity of the rolls. Despite this fact, we decided to neglect not only gravity but also inertial effects in order to keep the present model as simple as possible. Hence, the momentum and mass conservation equations are:

$$\nabla \cdot \mathbf{T} = 0,$$

$$\nabla \cdot \mathbf{v} = 0. \tag{3}$$

In Eq. (3), $\mathbf{T} = -p\mathbf{I} + (\nabla\mathbf{v} + \nabla\mathbf{v}^T)$ is the total stress tensor ($\mathbf{I}$ being the identity tensor), made dimensionless with $V_E\mu/\delta$. It should be noted that Eq. (3) is solved only on the liquid domain, which deforms as the upper plate separates from the cavity.

Because the surface tension is constant, the capillary force along the interface has only normal component, given by

$$\mathbf{n}_{fs} \cdot \mathbf{T} = \frac{\kappa}{Ca}\mathbf{n}_{fs}, \tag{4}$$

where $Ca = \mu V_E/\sigma$ is the capillary number and κ is the mean curvature of the free surface ($\kappa = -\nabla_s \cdot \mathbf{n}_{fs}$). In the above expression, $\nabla_s = (\mathbf{I} - \mathbf{n}_{fs}\mathbf{n}_{fs}) \cdot \nabla$ is the free surface gradient operator.

Along the walls, the fluid has the same normal velocity as the solid surface. In a similar manner, because the free surface is a material surface, the net flux across it vanishes. Thus, the following boundary conditions are used along each surface:

$\mathbf{v} \cdot \mathbf{n}_w = 0,$ at the cavity walls;

$(\mathbf{v} - \mathbf{V}_w) \cdot \mathbf{n}_w = 0,$ at the moving plate;

$\mathbf{n}_{fs} \cdot (\mathbf{v} - \dot{\mathbf{x}}) = 0,$ at free surfaces. $\qquad$ (5)

In Eq. (5), $\dot{\mathbf{x}}$ represents the velocity of the free surface. To overcome the stress singularity at the contact lines, we allow the fluid to slip along the tangential direction (Huh and Scriven, 1971). As in previous analysis (Ubal et al., 2012; Dodds et al., 2012; Campana and Carvalho, 2014), Navier-slip is considered along the solid walls and a contact angle between the liquid interface and solid walls is prescribed:

$(\mathbf{n}_w \cdot \mathbf{T}) \cdot \mathbf{I}_s = \beta^{-1}(\mathbf{I}_s \cdot (\mathbf{v} - \mathbf{v}_{surf}));$ $\mathbf{n}_w \cdot \mathbf{n}_{fs} = \cos(\theta_i);$ $i = c, p$ $\qquad$ (6)

In Eq. (6), β is the dimensionless slip coefficient as defined in Lamb (1975), $\mathbf{v}_{surf}$ is the velocity of the solid surface and $\mathbf{I}_s = (\mathbf{I} - \mathbf{n}_w \mathbf{n}_w)$ is the identity tensor on the solid surface.

A common approach is to consider the apparent dynamic contact angle θ_i to be a function of the contact line velocity (see Blake (2006) for a discussion of the available models). We follow here the simple approach used by Cairncross et al. (2000) and Dodds et al. (2012) and we use a linear dependence between the contact angle and contact line velocity:

$\cos\theta = \cos\theta_i^s - \gamma_f Ca\dot{x}_{wet};$

$\dot{x}_{wet} = (\mathbf{v} - \mathbf{v}_{surf}) \cdot \mathbf{t}_w$ $\qquad$ (7)

In Eq. (7), θ_i^s is the static contact angle of the contact line i and $\dot{x}_{wet}$ is the velocity of the contact line relative to the surface velocity in a direction tangent to the surface and normal to the contact line; this direction is represented by the unit vector $\mathbf{t}_w$. Finally, γ_f is a friction parameter which we set equal to zero: the dynamic contact angle is constant and equal to the static contact angle.

The above governing equations and their boundary conditions must be solved in an unknown deforming domain that must be calculated as part of the solution. The spatial deforming domain is mapped to a known fixed reference domain and the mapping function is solved simultaneously with the rest of the flow variables. The solution of the mapping function, with appropriate boundary conditions, gives the coordinates of the nodal positions for a given time step, from which the mesh can be updated to adjust the new configuration of the domain. There are several ways to construct the mapping, being the best choice strongly problem dependent. In this work we have tested pseudo-solid material (Cairncross et al., 2000) and Laplacian type methods such as the Winslow's technique used by Ubal et al. (2014). The later showed the best performance. If the coordinates of the nodal position on the fixed reference domain are designated as $\hat{\mathbf{X}}$, the Winslow's technique consists of calculating the displacement of the nodal position by solving the following partial differential equations

$\nabla^2 \hat{\mathbf{X}} = \mathbf{0},$ $\qquad$ (8)

where the ∇ operator is calculated in the spatial (physical) coordinates $\mathbf{x} = \mathbf{x}(\hat{\mathbf{X}}, t)$ and the nodes move with velocity $\dot{\mathbf{x}} = \partial \mathbf{x}/\partial t|_{\hat{\mathbf{X}}}$. Eq. (8) is solved with appropriate boundary conditions. We use the kinematic condition along the free surface (see Eq. (5)) to track the displacement of the moving surface, and the function given by Eq. (1) along the cavity walls to define its geometry. These are implemented using a Lagrange multiplier technique, that is briefly explained in the next section.

3. Numerical technique

The numerical methodology used in this work is a 3D extension of that used by Campana and Carvalho (2014) to solve 2D plane and axisymmetric flow problems. The main ideas were taken from Cairncross et al. (2000), Sprittles and Shikhmurzaev (2012) and Ubal et al. (2012) and then adapted to this particular problem. The weak form of the partial differential equations (3) and (8) are obtained in the usual form, then they are discretized with the finite element method and the flow domain is tessellated with an unstructured mesh of tetrahedrons. Quadratic Lagrange polynomials are used as basis functions to expand the velocity field and linear continuous basis functions to expand the pressure field (P2P1 tetrahedral elements). For the nodal displacement, Eq. (8), linear continuous functions (linear elements) are used to minimize the appearance of degenerated elements due to excessive mesh distortions.

The boundary conditions are implemented by the Lagrange multipliers technique. Its application to free surface flow problems is discussed in detail by Sprittles and Shikhmurzaev (2012). The key concept is that new degrees of freedom are introduced on boundaries where constraints must be applied and they are interpreted as stresses on the given surface. For example, the weak form of the momentum Eq. (3) is built by projecting the equation with the same set of basis functions φ^i used to interpolate the velocity field (Galerkin formulation); it reads:

$\int_{\Omega} (\nabla\varphi^i \cdot \mathbf{T}) \, d\Omega = \int_{\Gamma} \varphi^i (\mathbf{n} \cdot \mathbf{T}) \, d\Gamma.$ $\qquad$ (9)

To obtain Eq. (9) the divergence theorem was applied over the domain Ω with boundary $\Gamma = \Gamma_s + \Gamma_m + \Gamma_{fs}$, where Γ_s represents the fixed solid boundaries (cavity wall), Γ_m the moving solid boundaries (upper plate) and Γ_s the free surface.

The traction vector $(\mathbf{n}_{fs} \cdot \mathbf{T})$ along the free surface is directly substituted by the normal stress balance given by Eq. (4). This expression is integrated by parts once more, thus obtaining a contribution along the free surface itself and a line integral along the contact lines. This last expression is used to impose the contact angle (see Sprittles and Shikhmurzaev (2012) for details).

The traction vector for the fluid on solid surfaces $(\mathbf{n}_w \cdot \mathbf{T})$ is handled in a different way. It is decomposed in normal and tangential directions (see Eq. (6)):

$(\mathbf{n}_w \cdot \mathbf{T}) = (\Lambda_w)\mathbf{n}_w + \beta^{-1}(\mathbf{I}_s \cdot (\mathbf{v} - \mathbf{v}_{surf}))\mathbf{t}_w;$

$\Lambda_w \equiv (\mathbf{n}_w \cdot \mathbf{T} \cdot \mathbf{n}_w)$ $\qquad$ (10)

In Eq. (10), Λ_w is a Lagrange multiplier representing the normal stress to the solid boundaries (cavity wall and moving plate). Λ_w is approximated as a new finite element variable field and is written as a linear combination of two-dimensional basis functions $\tilde{\varphi}^i$ defined along the solid surfaces. To calculate the new degrees of freedom Λ_w^j, the kinematic condition (Eq. (5)) is imposed as a new weighted residual: $\int_{\Gamma_s} \tilde{\varphi}^i (\mathbf{v} \cdot \mathbf{n}_w) \, d\Gamma = 0$ is used on the fixed wall and $\int_{\Gamma_m} \tilde{\varphi}^i [(\mathbf{v} - \mathbf{V}_w) \cdot \mathbf{n}_w] \, d\Gamma = 0$ on the moving plate. With this approximation, Λ_w represents the normal stress on the solid boundary that must be applied to the fluid in order to satisfy the kinematic condition.

A similar approach is used for Eq. (8) that describes the nodal displacement. Once its weak form is obtained and the corresponding term is integrated by parts, the normal component of the pseudo-traction vector acting on the boundary is defined as a new Lagrange multipliers field. Along the cavity wall, the normal nodal displacement is restricted by a pseudo-stress along the boundary so that Eq. (1) is satisfied. The pseudo-stress satisfies $\int_{\Gamma_m} \tilde{\varphi}^i [(\dot{\mathbf{x}} - \mathbf{V}_w) \cdot \mathbf{n}_w] \, d\Gamma = 0$ and $\int_{\Gamma_{fs}} \tilde{\varphi}^i [(\dot{\mathbf{x}} - \mathbf{v}) \cdot \mathbf{n}_{fs}] \, d\Gamma = 0$ along the

moving plate and the free surface, respectively. There are no restrictions on the tangential directions and nodes can freely move to minimize mesh distortions.

The aforementioned approach has the advantage that non-linear boundary conditions (as Eq. (1)) can be applied in a very clean and easy way; however, its drawbacks are that new degrees of freedom are introduced and the size of the computational problem increases. This is specially important in our approach because we solve the resulting non-linear system of algebraic equations obtained from the implicit time integration using a fully coupled solver: velocity, pressure and nodal displacements (mesh deformation) are simultaneously calculated. Previous numerical experiments (Dodds et al., 2012; Campana and Carvalho, 2014) show that this approach, combined with the use of sparse direct solvers, improves the robustness of the technique allowing better convergence and numerical stability. Thus, the level of discretization used is the result of a balance between computer execution time and solution accuracy; a typical mesh meeting this requirement has approximately 100,000 elements and 600,000 degrees of freedom.

The aforementioned weak forms of the governing equations and the resulting set of Lagrange multipliers fields are solved with the commercial finite element software COMSOL Multiphysics (COMSOL Multiphysics, 1998-2013). A fully implicit second order time integration scheme with adaptive time step is used and all variables are simultaneously calculated at each time step. As we mentioned before, this fully-coupled scheme shows better convergence and stability properties compared to others decoupled or semi-implicit numerical procedures. At each time step, the resulting set of non-linear equations is solved using Newton's method. During the evolution of the liquid filament, the liquid domain largely deforms and the elements become distorted; hence, the accuracy of the solution is compromised. To control the mesh quality, the aspect ratio of each element is computed during the transient calculation. Whenever this control parameter goes below a critical value, the simulation is stopped. Then, the domain configuration of the last converged solution is used to define a new geometry (and reference configuration), which is tessellated into a new, high-quality mesh of tetrahedrons. The last converged solution is interpolated onto the new mesh and the time integration resumed. Typically, the simulations presented here require (depending on Ca) between 8 and 20 stages of re-meshing to complete the run. Since there is an inherent error in each geometry re-construction and further re-meshing procedures, we use the total volume of the liquid bridge as a control variable in order to check the error associated with them. In this way, we are certain that the maximum variation between the initial and the breakup liquid volumes does not exceed 0.1%.

4. Results

This section is organized as follows. The validation of the numerical procedure is presented in Section 4.1, the effect of the capillary number on the transferred liquid fraction is studied in Section 4.2 and finally, the influence of the capillary number on the printed pattern is explored in Section 4.3.

4.1. Validation

In our computations the number of degrees of freedom was kept close to 600,000. However, this implies that near the contact lines (where there are large velocity gradients) the mesh was comparatively coarser than those previously used to solve 2D plane and axisymmetric models (Sprittles and Shikhmurzaev, 2012; Campana and Carvalho, 2014). Therefore, we first recomputed numerical solutions

of the axisymmetric case but using the 3D numerical model described in the previous section. These predictions were compared to the predictions computed with a previous 2D axisymmetric numerical model (Campana and Carvalho, 2014). In fact, in the 3D model the size of the elements near the contact line was $O(10^{-2})$, that is, two orders of magnitude larger than the elements used in the 2D axisymmetric flow analysis. To preserve the symmetry of the flow, we employed a one-dimensional simplification of the plate velocity given by Eq. (2) that results in a vertical motion (Campana and Carvalho, 2014). The plate velocity is

$$\mathbf{V}_w(\mathbf{x}, t) = -2\omega R_b \cos(\theta)\mathbf{k} \qquad (11)$$

The plate velocity given by Eq. (11) was used to run both the axisymmetric and 3D models. The values of the geometric and flow parameters correspond to the reference case (RC) used by Campana and Carvalho (2014). These parameters were chosen considering typical values of gravure printing operating conditions, geometric parameters and liquid properties: roll radius $R = 6$ in $= 0.1524$ m, cavity depth $\delta = 10$ μm, cavity width $R_c = 8$ μm, roll and substrate speed $\Omega R = 10$ m/s, liquid viscosity $\mu = 0.02$ Pa s and surface tension $\sigma = 0.025$ N/m. The contact angles were set to $\theta_c = \theta_p = 70°$. The slip coefficient β defines the region close to the contact lines at which slip is significant and the actual value of the contact line velocity. $\beta \equiv l/\delta$ is determined by considering the dimensional slip length range $1 \leq l \leq 10$ nm, resulting in $10^{-4} \leq \beta \leq 10^{-3}$. In the parametric analysis presented by Campana and Carvalho (2014), values of $\beta > 10^{-2}$ led to unrealistic large-slip regions, while $\beta < 10^{-3}$ required highly refined meshes without significant changes in the solution. Thus, here we set $\beta = 10^{-3}$. The values of the model parameters are summarized in Table 1.

Fig. 4 depicts the free surface position in the $z - y$ plane for both the 3D and the axisymmetric model at the same dimensionless time $t = 3.46$. These free surface profiles correspond to the last time a solution without excessive mesh distortion could be obtained with the 3D model. The filament configurations predicted by both models are close, however the contact line positions on the moving substrate differ by around 8%. If this discrepancy is acceptable or not will depend on the application and the expected reliability of the results. In this work we are mainly interested in a estimation of the transferred liquid fraction ϕ and, as we show next, the predicted values of ϕ are almost coincident for both models.

Although 3D solutions could not be obtained for $t > 3.46$, the evolution of the liquid bridge in the axisymmetric model continued up to the instant at which the minimum radius of the filament reached the value $r_b = 0.03$, at z_b. This was arbitrarily taken as the breakup time and denoted as t_b. For this particular case, $t_b = 3.56$ and the predicted 2D axisymmetric free surface profile at this time is also shown in Fig. 4. To estimate the transferred liquid fraction in the 2D flow, we computed the liquid volume V_p for $z > z_b$ and $\phi = V_p/V_t = 0.058$, being V_t the total liquid volume. Because the 3D simulation could not be continued for $t > 3.46$, we used spline extrapolation of the 3D predictions to determine the

Table 1
Values of the model parameters corresponding to the reference case (RC).

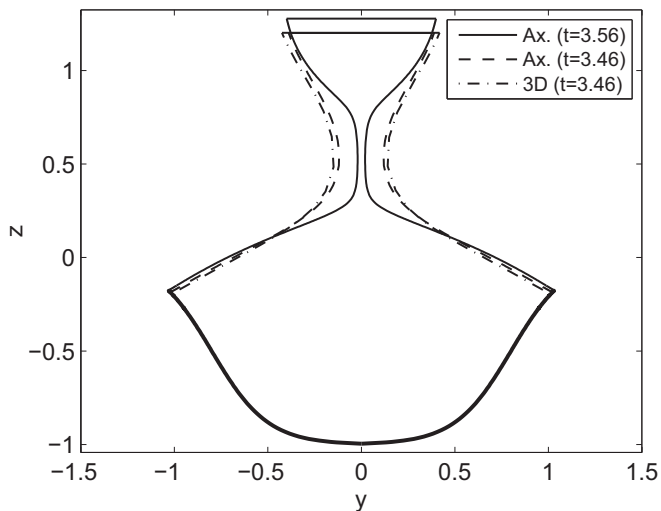|		
Capillary number	Ca	0.1
Roll radius to cavity depth ratio	R_b	15,240
Dimensionless angular speed	ω	2.5×10^{-3}
Gap to cavity depth ratio	H_b	0.03
Cavity width to depth ratio	r_c	0.8
Cavity geometry parameter	r_s	0.3
Slip coefficient	β	10^{-3}
Contact angles	$\theta_p^s = \theta_c^s$	70°
Contact line friction parameter	γ_f	0

Fig. 4. Validation of a 3D simulation without rotation ($Ca = 0.1$, $R_b = 15$, 240) with its equivalent axisymmetric case (Ax.), which was obtained with a much more refined mesh at the contact line.

breakup time, defined such that $r_b = 0.03$, as indicated in Fig. 5a, and the transferred liquid fraction, as indicated in Fig. 5b. With this procedure, the breakup time and the transferred liquid volume predicted by the 3D model are $t_b \sim 3.71$ and $\phi \sim 0.059$, respectively. Note that these values are very close to the predictions of the axisymmetric model. Since this procedure led to very good agreement between predictions of both models in all similar tests performed for Ca between 0.01 and 0.1, we used this approach to predict the values of ϕ for all 3D simulations.

In the next sections we studied the effect of capillary number and roll radius on the volume of liquid transferred to the substrate and on the printing pattern. The goal was to understand how the 3D character of the flow changes the capillary pressure field, which is the driving force for filament breakup, and the contact line motion. We did not explore the effects that cavity geometries and wetting properties might have on the process; nonetheless, it was shown (Dodds et al., 2009) that for a pure extensional relative motion, the cavity aspect ratio and contact angle differences between the surfaces change the liquid volume removed from the cavity. These effects should still be relevant for complex kinematics, such as the one analyzed here, and are left for future analysis.

4.2. Effect of capillary number and roll radius on the transferred liquid fraction

Fig. 6 depicts a comparison between the values of ϕ obtained for full 3D motion and those obtained for axisymmetric motion. The predictions in the first case were calculated with the 3D flow model using the complete R2R kinematics given by Eq. (2), while in the last case they were obtained with the 2D axisymmetric model (labeled Ax. in the plot) because, as we showed in the previous section, the values of ϕ are in good agreement with the 3D model that only considers vertical motion. It can be observed that for the pure stretching motion (Ax.), ϕ diminishes monotonically as Ca falls. This behavior was explained in detail in Campana and Carvalho (2014), by analyzing the mobility of the contact lines (along the cavity and plate surfaces) as a function of the capillary pressure gradient. As the capillary number increases, the contact line motion along the surfaces slows down and the size of the liquid drop at the substrate enlarges resulting in larger values of ϕ.

Results reported in Fig. 6 show that even though calculated values of ϕ for the full R2R kinematics follow the behavior of the
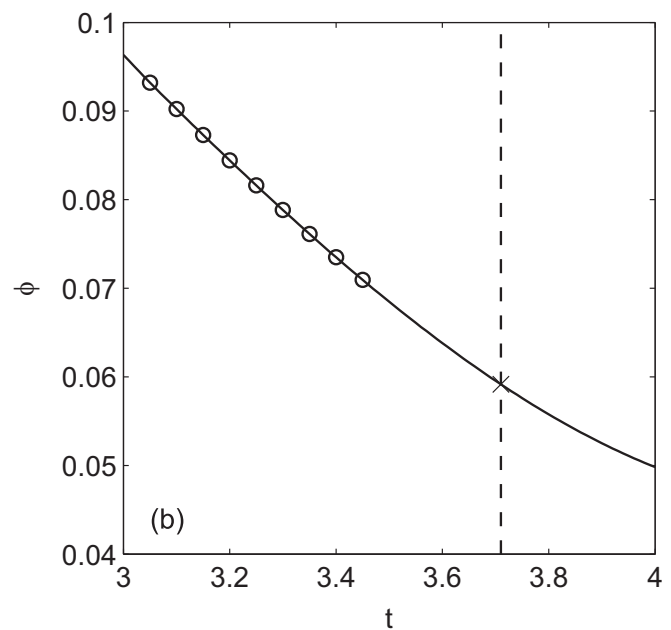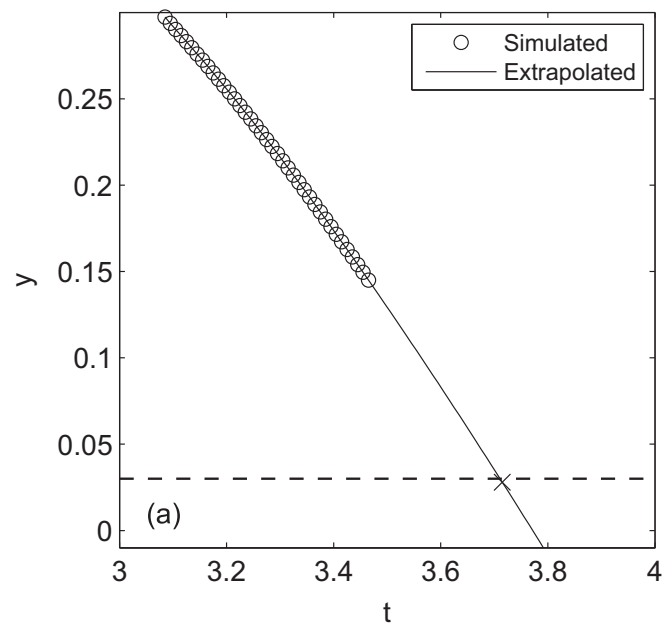

Fig. 5. (a) Evolution of the y coordinate of the point with minimum thickness in the liquid filament; circles represent results of the simulation, dashed line is the filament radius (r_b) at the imposed breakup time and the continuous line the spline extrapolation. (b) Evolution of the calculated liquid fraction for selected times; continuous line also represents the spline extrapolation.

stretching motion case for $Ca > 0.02$; however, the behavior at lower capillary numbers is quite different. The variation of the transferred volume with Ca for the complete R2R kinematics can be better understood by analyzing the free surface evolution at $Ca = 0.01$, shown in Fig. 7. At low capillary number, the R2R kinematics leads to a flow at which the liquid bridge is pushed out of the cavity and the whole contact line is located on the flat surface for $t > 2.8$. At this stage, the evolution continues as a liquid bridge being stretched between two flat surfaces. During the evolution outside the cavity, a neck on the liquid filament begins to form on a region closer to the cavity and consequently, after the breakup, more liquid remain on the portion attached to the moving plate; thus, $\phi \sim 0.65$ at $t \sim 5.0$. This process is similar but even stronger at $Ca = 0.0125$, at which $\phi \sim 0.8$.
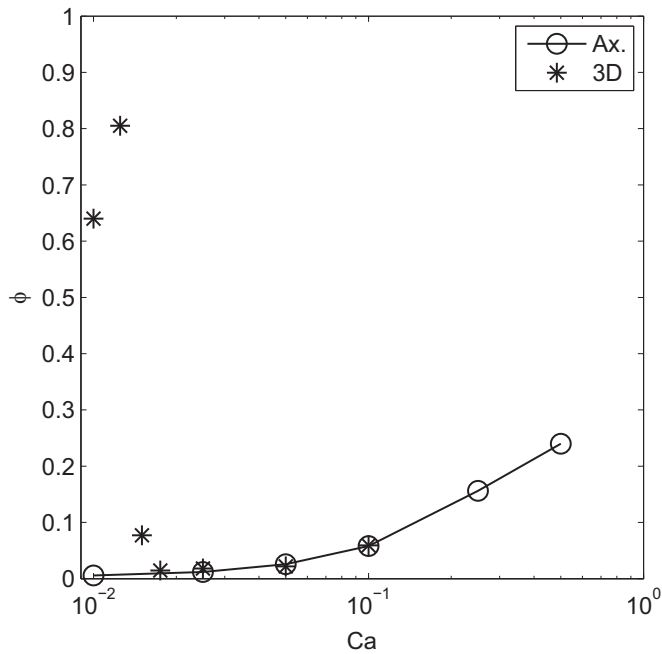
Fig. 6. Transferred liquid fraction versus *Ca* for both 3D and axisymmetric simulations. The rest of parameters correspond to the RC.

The behavior of the 3D flow is similar to the one observed in the case of liquid transfer from an infinite groove (2D planar flow) analyzed by Campana and Carvalho (2014) and can be summarized as follows. The dynamics of the liquid transfer is governed by two different characteristic times. One is related to the motion of the contact lines along the surfaces, which is a function of the capillary pressure gradient; the other is related to the filament breakup time, which depends on the velocity at which roll surfaces are separating and thereby controlling the formation of the filament neck. If the liquid filament is pushed out of the cavity much faster than the roll surfaces are getting apart, the neck will begin to form between two flat surfaces. In agreement with previous results (Campana and Carvalho, 2014; Dodds et al., 2012), this situation usually leads to $\phi \sim 0.5$ (see Fig. 6 for $Ca < 0.01$). On the other hand, if the filament neck is formed sufficiently fast, while the cavity contact line is still inside of it, ϕ increases with *Ca* and the flow is well approximated by the stretching kinematics; this behavior is observed at $Ca > 0.02$. Between the two regions, a more complex situation appears: if the neck is formed while the cavity contact line is slipping over the cavity corner, as for $Ca = 0.0125$ and 0.01, more liquid is transferred to the plate because the filament breaks in its lower half part (closer to the cavity).

It is very interesting that ϕ versus *Ca* presents the same non-monotonic behavior in both the 2D planar flow analyzed by Campana and Carvalho (2014) and the full 3D flow here discussed. However, the values of ϕ are quite different because in the latter
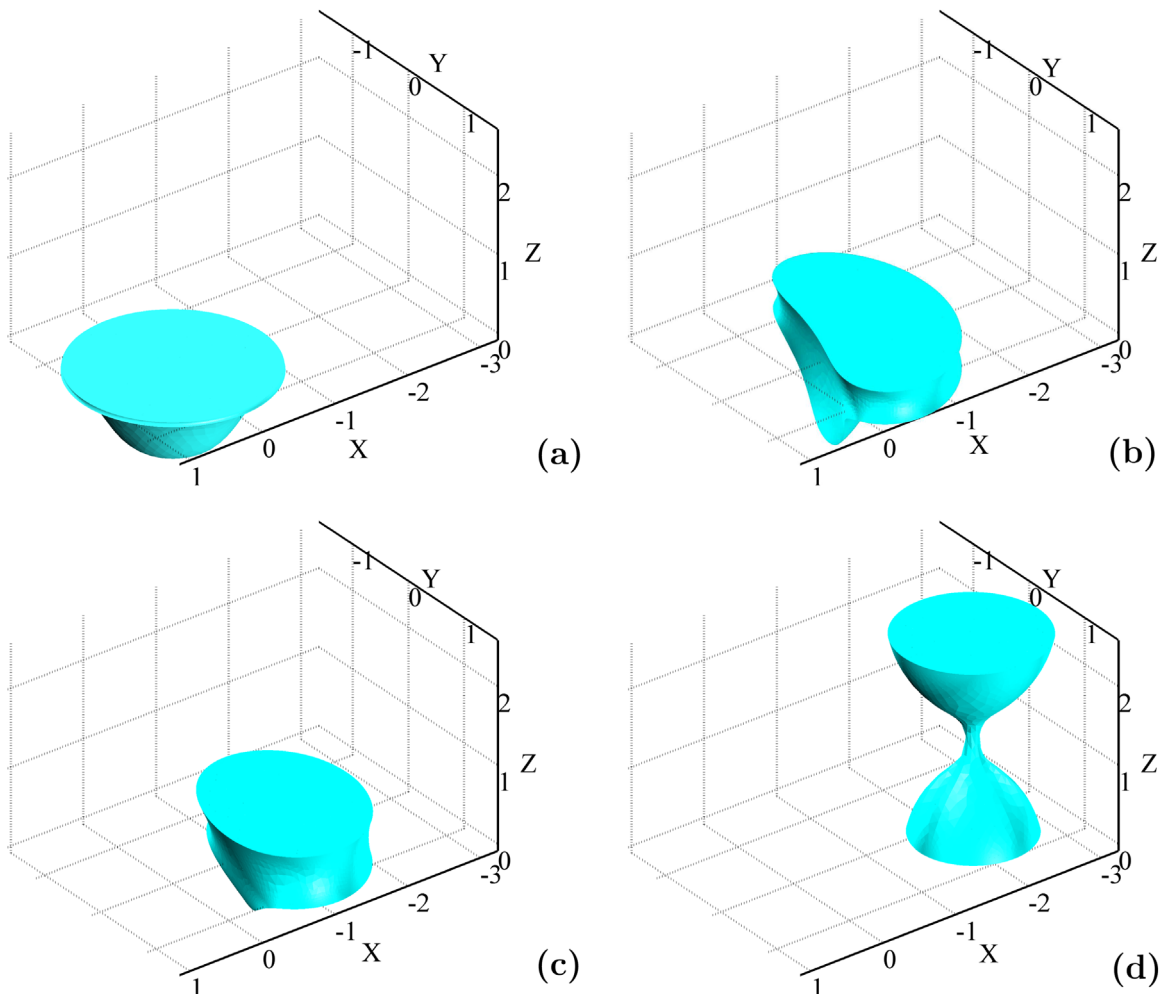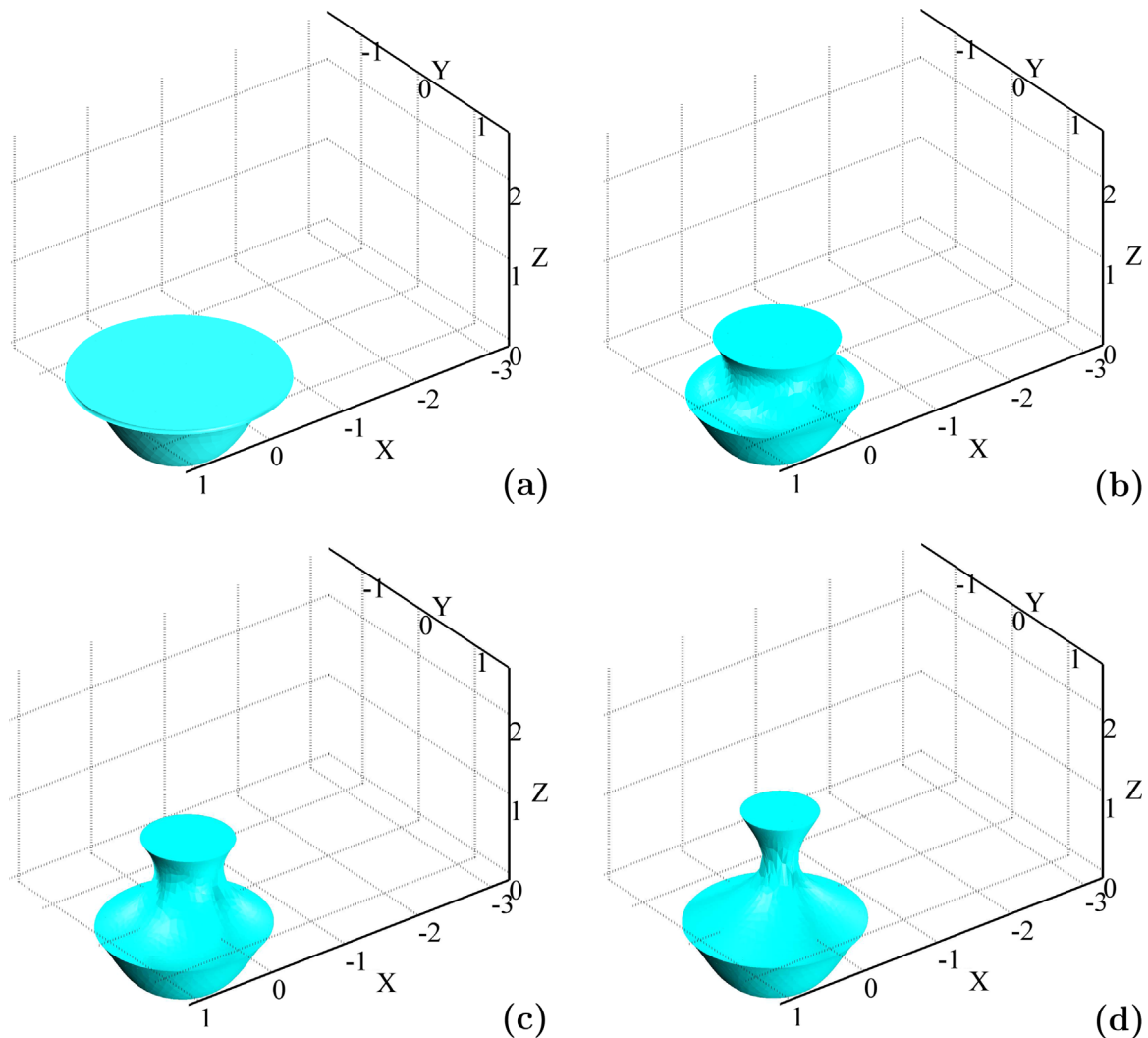

Fig. 7. Snapshots of the evolution in the liquid transfer at $Ca = 0.01$; the rest of the parameters correspond to the RC. (a) $t = 0$, (b) $t = 2.00$, (c) $t = 2.57$ and (d) $t = 5.00$. The center of the cavity is located at $x = y = 0$.

Fig. 8. Snapshots of the evolution in the liquid transfer at $Ca=0.1$; the rest of the parameters correspond to the RC. (a) $t=0$, (b) $t=2.00$, (c) $t=2.85$ and (d) $t=3.36$. The center of the cavity is located at $x = y = 0$.

case, the capillary pressure and consequently the breakup is dominated by the azimuthal curvature which is not present in the plane model. The higher pressure gradient in the neck accelerates the breakup of the liquid filament, reducing the time available to remove liquid from the cavity. Consequently, the amount of liquid transferred to the substrate is smaller in the case of a cavity (3D) than in the case of a groove (plane 2D). At $Ca \sim 0.05$, $\phi \sim 0.022$ for the 3D flow and $\phi \sim 0.38$ for the 2D plane flow. The evolution of the free surface for $Ca=0.1$ is shown in Fig. 8; at this capillary number, the neck is formed before the contact line moves out of the cavity. The strong pressure gradient in the neck pumps liquid back to the cavity leading to a low liquid transfer fraction ϕ.

Due to the velocity scale chosen, ω is proportional to $R_b^{-1/2}$ and thus a reduction in the roll size promotes a larger rotational and horizontal dimensionless velocities of the plate relative to the cavity. In the 2D plane flow, Campana and Carvalho (2014) showed that this has an important effect on ϕ, which increases almost linearly with a reduction of R_b. For example, ϕ rises by 25% as R_b decreases from 15,240 to 2540, keeping all the other dimensionless parameters the same. In the present full 3D analysis, ϕ increases approximately 12% as the roll size falls (with all the other dimensionless parameters fixed): $\phi = 0.059$ for $R_b=15,240$ and $\phi = 0.0675$ for $R_b=2540$. This indicates that as a consequence of the faster breakup of the filament, the 3D flow is less sensitive

than the 2D plane flow to increments in the rotational and horizontal velocity. At lower capillary number, e.g. $Ca=0.05$, the increment in ϕ is higher (approximately 37%): $\phi = 0.022$ for $R_b=15,240$ and $\phi = 0.0353$ for $R_b=2540$. It is important to note that the characteristic velocity V_E used in the definition of the capillary number is a function of the roll diameter. Therefore, changes on roll diameter actually affect both R_b (and consequently ω) and Ca.

In summary, the predictions for ϕ versus capillary number and roll radii obtained with the 3D flow model show the same qualitative behavior as the one obtained with the 2D planar flow model. However the results are not directly comparable because the values of ϕ and its sensitivity to changes in R_b are remarkably reduced. As was discussed, this is a consequence of the azimuthal curvature of the filament in the 3D flow processes that accelerates the breakup.

In contrast, Fig. 6 shows that for $Ca > 0.02$ differences between the full 3D and the 2D axisymmetric computations are negligible. Furthermore, these differences are also negligible for the highest rotational velocities here considered ($R_b=2540$). These results demonstrate that to solve a full 3D flow model with a complete R2R kinematic is not required within this Ca range, because in these situations the contact line slipping promoted by the shear velocities is small and thus, there is no appreciable effect on the transferred liquid fraction. In other words, in this range of the

capillary number a 2D axisymmetric model using only stretching kinematics would be sufficient to obtain accurate predictions. As we mentioned, Dodds et al. (2009) explored a wide range of cavity sizes and contact angle differences using this approach. Our results suggest that their predictions accurately describe the liquid volume transferred in a R2R system if the capillary number is high enough.

Because the results were obtained just for one cavity shape and a contact angle value (see Table 1), the question is if the conclusions can be extended to other conditions. As long as the velocity of separation of the surfaces, which controls the filament breakup, is higher than the contact line velocity (high Ca), we should expect the same qualitative behavior of the fraction ϕ versus the capillary number for different cavity aspect ratios. However, when the dynamic contact line velocity becomes more important than the velocity of separation of the surfaces (small Ca), wetting properties and contact angles will influence significantly the results. This dependence was not explored in the present work.

4.3. The influence of capillary number in the printed pattern

For the conditions explored in this work, our results suggest that high liquid transfer ratio can only be obtained at low enough capillary number, e.g. $Ca < 2 \times 10^{-2}$. However, low capillary numbers lead to a high contact line mobility along both the cavity surface and the substrate. The pronounced contact line slipping might produce poor results concerning fidelity and registration (precision placement of the printing pattern). Because the substrate is moving, the contact line configuration is presented in a moving frame of reference attached to the substrate, denoted by the (x_*, y_*) coordinates in Fig. 3. Fig. 9 shows the contact line configuration (printed pattern) on the substrate close to the breakup point at different capillary numbers. In the moving frame of reference, a perfectly registered pattern should be centered at $x_* = y_* = 0$. The initial contact line configuration (at $t=0$) is also shown in Fig. 9 as a reference (thicker line). At high capillary numbers, e.g. $Ca=0.1$, the printed dot area is approximately 13% of the initial area and its center is located close to $x_* = y_* = 0$. As the capillary number decreases, the printed pattern area does not

change considerably, but it is shifted towards $x_* < 0$. At the lower capillary number explored, e.g. $Ca=0.01$, the pattern is much larger, 58% of the initial area, and its position indicates loss of registration in the x^* and y^* directions. It is important to note that the substrate kinematics is independent of the y-coordinate. The loss of registration in the y direction results from small perturbations in the flow triggered by the numerical procedure. At low capillary number the contact line slipping is strong, the printed pattern moves away from its initial position on the substrate and it even loses its circular shape.

Darhuber et al. (2001) carried out experiments and quasi-static simulations in order to uncover the physical mechanisms controlling the pattern fidelity in offset printing operations. They prepared hydrophilic surface patterns on a hydrophobic surface enabling the deposit of ink following specific designed shapes. Because they used smooth non-porous surfaces like those modeled in this work, important contact line displacements were observed. Their experiments showed that the unwanted ink redistribution after printing can be minimized by using higher viscosity ink. Based on their simulations, they suggested that the receding of the contact lines during printing can be reduced by increasing the plate vertical separation velocity. An increase in either ink viscosity or separation velocity means in both cases an increase in the capillary number, which is in qualitative agreement with our results shown in Fig. 9.

The shape distortion of the printed pattern can be characterized by the circularity C of the pattern. This quantity is measured as the ratio of the perimeter of a circle that has the same area A of the pattern and the calculated contact line length L; i.e., $C = 2\pi L^{-1}\sqrt{A/\pi}$. Thus, if the pattern is a circle then $C=1$; otherwise, $C < 1$. Fig. 10 shows the evolution of C for the conditions shown in Fig. 9. For $Ca < 0.1$ the contact line strongly distorts from its original circular shape as the liquid moves out of the cell: then, capillary pressures nearly restores its original circular shape. For the lowest capillary number explored ($Ca=0.01$), the final value of C (at the liquid breakup) is $C=0.998$. The shapes of the contact line on the substrate for the minimum values of C computed for four different values of the capillary number are presented in Fig. 11 as examples. As we mentioned, at low capillary number the liquid bridge moves out of the cell and during this process the printed pattern is strongly distorted, becoming concave on one side.
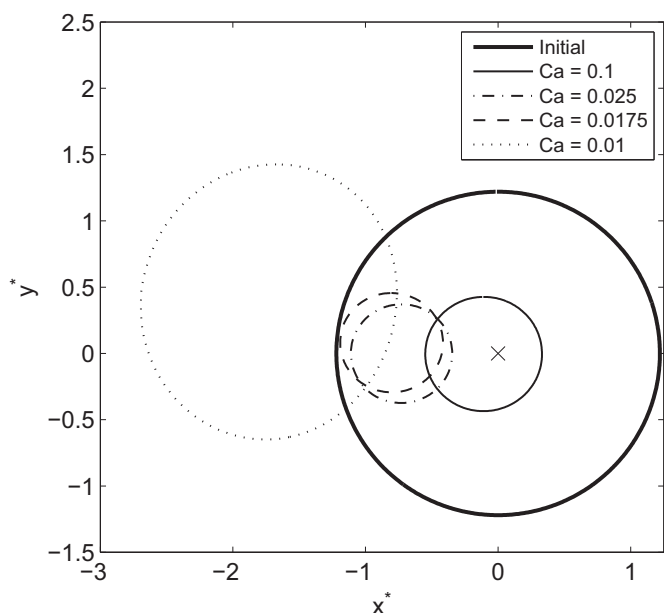

Fig. 9. Contact line positions on the substrate at the last simulated time. The thicker line labeled as *Initial* represents the contact line at $t=0$, which is the same for all cases.
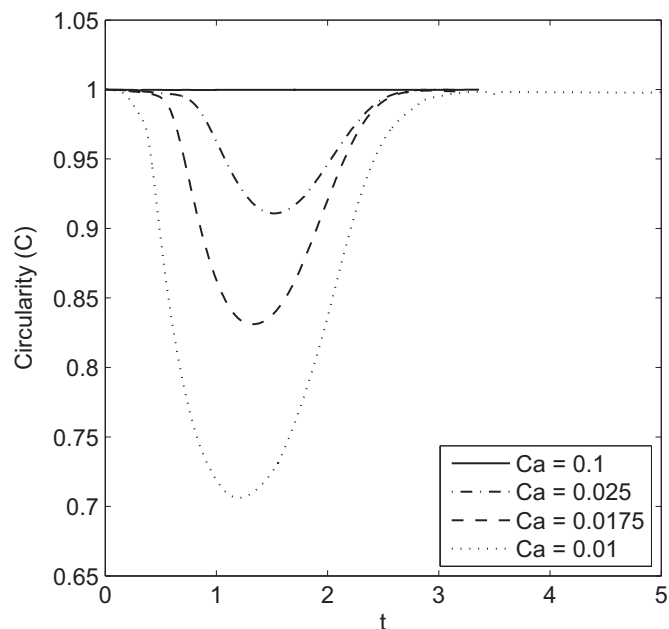

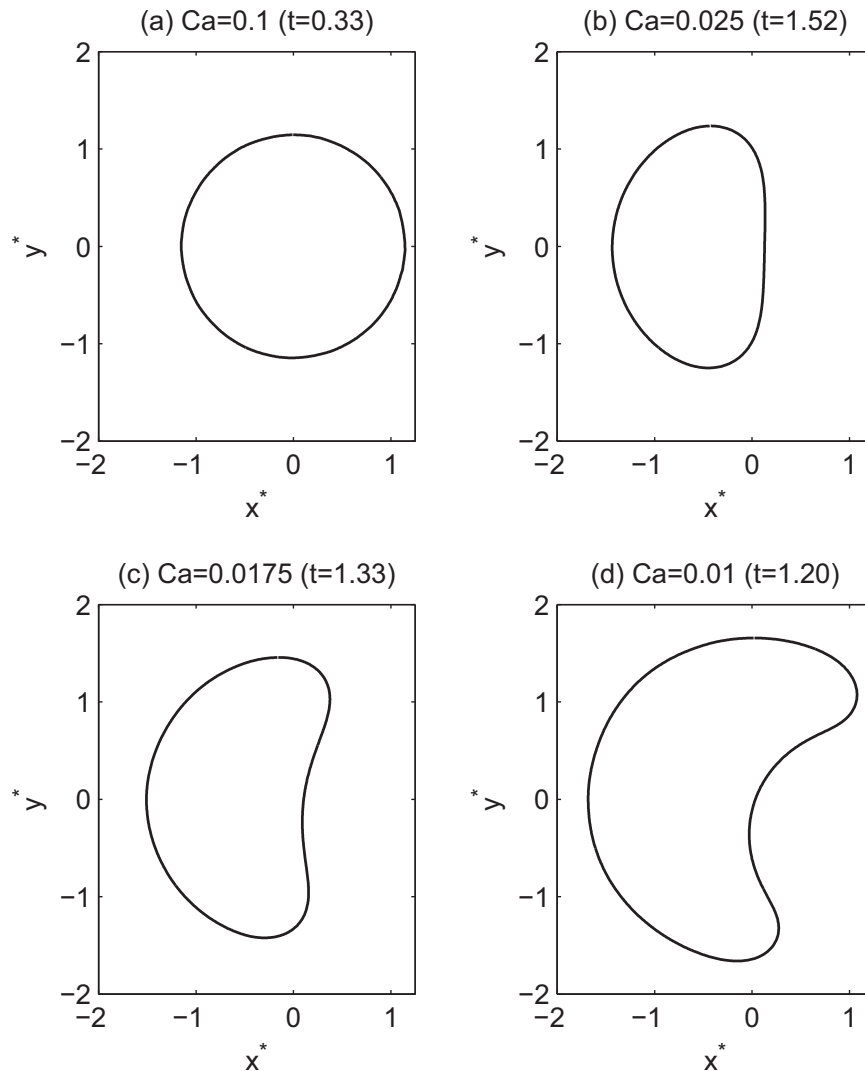**Fig. 10.** Evolution of the pattern circularity C for several Ca.

Fig. 11. Position of the contact lines on substrate at the instant of minimum circularity C.

The contact line mobility and consequently the printing pattern configuration are likely to be highly dependent on the contact angles and slip parameters. Therefore, the printing pattern size and placement will vary with the wetting characteristics of both surfaces. The effect of these parameters were not explored here and remains to be studied.

5. Conclusions

The fundamental aspects of gravure printing can be better understood by analyzing the liquid transfer from a single cell to a substrate wrapped around a rotating roll. Previous numerical analyses either considered a simplified relative motion between the cell and the substrate or were restricted to a 2D planar flow that described liquid transfer from an infinite groove, not a cell. Therefore, these analyses cannot be readily used to determine not only the amount of liquid transferred to the substrate but also the characteristics of the printing pattern.

In this work, we extended our previous analysis to fully describe the 3D free surface flow with moving contact lines that occurs during the liquid transfer process. As in liquid transfer from infinite grooves (2D plane flow), the process can only be accurately described by considering the complete kinematics between a rotating roll and the liquid-filled cell. The amount of liquid transferred to the substrate is a function of the ratio between two characteristic time scales, one related to the contact line motion and the other to the filament breakup. Both phenomena are strongly dependent on capillary number and, for the situation here explored, the results can be summarized as follows.

At low capillary number ($Ca < 10^{-2}$), the contact lines are very mobile and the liquid is pushed out of the cavity before the filament breakup. In these cases, the amount of liquid that is transferred to the substrate is higher than 50% of the cavity volume. On the other hand, at intermediate capillary numbers (2×10^{-2} to 10^{-1}), the contact lines are less mobile and breakup occurs before the liquid is pushed out of the cell. Then the amount of liquid transferred to the substrate decreases to values lower than 5% of the cell volume. At even higher capillary numbers, the transferred liquid volume increases as capillary number rises, mainly because the contact lines remain almost static during the process.

When the contact line mobility is low, the effect of the shear and rotational relative motion between the cell and the substrate is weak and the transferred liquid fraction is well described by simpler 2D axisymmetric model. This indicates that the 2D axisymmetric solutions presented by Dodds et al. (2009) for a wide range of cavity aspect ratios and contact angle differences accurately describe liquid transfer in a roll-to-roll configuration, if the capillary number is high enough. On other hand, when the

mobility of the contact lines is high, the relative motion between the surfaces strongly affects the way the liquid filament breaks up and the simpler 2D axisymmetric model underpredicts the transferred liquid ratio.

The 3D solutions presented here also reveal that although high liquid transfer ratio can be attained at low capillary numbers, the precision in the position of the printing pattern is poor when the contact lines are very mobile. Smaller dots with higher placement precision (improved registration) are obtained at high capillary numbers.

It is important to mention that the design of the process should not be guided only by conditions favoring the emptying of the cavities because, before that, the cavities must be filled. As was shown by Cen et al. (2014), at high capillary numbers, the contact line pins at the cavity corners slowing down the liquid filling step and promoting air entrapment inside the cavity. Thus, the optimal capillary number for a given process should be estimated considering all the phenomena just discussed: cavity filling, cavity emptying and registration of the pattern.

Acknowledgments

References

Baer, T.A., Cairncross, R.A., Schunk, P.R., Rao, R.R., Sackinger, P.A., 2000. A finite element method for free surface flows of incompressible fluids in three dimensions. Part II. Dynamic wetting lines. Int. J. Numer. Methods Fluids 33, 405–427.

Blake, T.D., 2006. The physics of moving wetting lines. J. Colloid Interface Sci. 299 (1), 1–13.

Cairncross, R.A., Schunk, P.R., Baer, T.A., Rao, R.R., Sackinger, P.A., 2000. A finite element method for free surface flows of incompressible fluids in three dimensions. Part I. Boundary fitted mesh motion. Int. J. Numer. Methods Fluids 33, 375–403.

Campana, D., Carvalho, M., 2014. Liquid transfer from single cavities to rotating rolls. J. Fluid Mech. 747, 545–571.

Cen, J., Kitsomboonloha, R., Subramanian, V., 2014. Cell filling in gravure printing for printed electronics. Langmuir 30 (45), 13716–13726.

Chuang, H.-K., Lee, C.-C., Liu, T.-J., 2008. An experimental study of the pick-up of scaled-up gravure cells. Int. Polym. Process. 23, 216–222.

COMSOL Multiphysics, 1998–2013. Comsol, URL ⟨http://www.comsol.com/⟩.

Darhuber, A.A., Troian, S.M., Wagner, S., 2001. Physical mechanisms governing pattern fidelity in microscale offset printing. J. Appl. Phys. 90 (7), 3602–3609.

Dodds, S., Carvalho, M.S., Kumar, S., 2009. Stretching and slipping of liquid bridges near plates and cavities. Phys. Fluids 21, 092103.

Dodds, S., Carvalho, M.S., Kumar, S., 2011. Stretching liquid bridges with moving contact lines: the role of inertia. Phys. Fluids 23, 092101.

Dodds, S., Carvalho, M.S., Kumar, S., 2012. The dynamic of three-dimensional liquid bridges with pinned and moving contact lines. J. Fluid Mech. 707, 521–540.

Hoda, N., Kumar, S., 2008. Boundary integral simulations of liquid emptying from a model gravure cell. Phys. Fluids 20, 092106.

Huh, C., Scriven, L.E., 1971. Hydrodynamic model of steady movement of a solid/liquid/fluid contact line. J. Colloid Interface Sci. 35, 85–101.

Kang, B., Lee, W.H., Cho, K., 2013. Recent advances in organic transistor printing processes. ACS Appl. Mater. Interfaces 5 (7), 2302–2315.

Krebs, F., 2009. Fabrication and processing of polymer solar cells: a review of printing and coating techniques. Sol. Energy Mater. Sol. Cells 93, 394–412.

Kumar, S., 2015. Liquid transfer in printing processes: liquid bridges with moving contact lines. Annu. Rev. Fluid Mech. 47, 67–94.

Lamb, S.H., 1975. Hydrodynamics, sixth ed. Cambridge University Press, London, UK.

Lee, C., Hu, S.H., Liu, T.J., Tiu, C., 2012. Three-dimensional observation on the liquid emptying process from a scaled-up gravure cell. Int. Polym. Process. 27, 128–137.

Lee, J.A., Rothstein, J.P., Pasquali, M., 2013. Computational study of viscoelastic effects on liquid transfer during gravure printing. J. Non-Newton. Fluid Mech. 199, 1–11.

Powell, C.A., Savage, M.D., Guthrie, J.T., 2002. Computational simulation of the printing of newtonian liquid from a trapezoidal cavity. Int. J. Numer. Methods Heat Fluid Flow 12 (4), 338–355.

Sankaran, A.K., Rothstein, J.P., 2012. Effect of viscoelasticity on liquid transfer during gravure printing. J. Non-Newton. Fluid Mech. 175, 64–75.

Sprittles, J.E., Shikhmurzaev, Y.D., 2012. Finite element framework for describing dynamic wetting phenomena. Int. J. Numer. Methods Fluids 68, 1257–1298.

Ubal, S., Grassia, P., Campana, D.M., Giavedoni, M.D., Saita, F.A., 2014. The influence of inertia and contact angle on the instability of partially wetting liquid strips: a numerical analysis study. Phys. Fluids 26 (3).

Ubal, S., Xu, B., Derby, B., Grassia, P., 2012. Continuous deposition of a liquid thread onto a moving substrate. Numerical analysis and comparison with experiments. J. Fluids Eng. 134 (2), 021301.

Willmann, J., Stocker, D., Dörsam, E., 2014. Characteristics and evaluation criteria of substrate-based manufacturing. Is roll-to-roll the best solution for printed electronics? Org. Electron. 15 (7), 1631–1640.

Yin, X., Kumar, S., 2006. Flow visualization of the liquid-emptying process in scaled-up gravure grooves and cells. Chem. Eng. Sci. 61, 1146–1156.